Oxygen Nonstoichiometry in $Sr_4Fe_6O_{13-\delta}$: The Derivatives $[Sr_8Fe_{12}O_{26}]\cdot[Sr_2Fe_3O_6]_n$

B. Mellenne, R. Retoux,* C. Lepoittevin, M. Hervieu, and B. Raveau*

Laboratoire CRISMAT, UMR 6508 CNRS ENSICAEN, 6 bd Maréchal Juin, 14050 Caen Cedex 4, France

Received March 22, 2004. Revised Manuscript Received June 14, 2004

Different samples of the ferrite "$Sr_4Fe_6O_{13}$", synthesized in air, nitrogen, and argon, have been studied by high-resolution electron microscopy. It is shown that this oxide is oxygen-deficient, i.e., $Sr_4Fe_6O_{13-\delta}$, and that its structure is modulated. The electron diffraction study shows that the modulation vector is $p\vec{a}^* + q\vec{c}^*$, with $p = (1 - \delta)/2$ varying in the range [0.4−0.5] and q close to 1. It is shown that the component of the modulation vector along $\vec{c}$ induces complex modulated structures. It is also demonstrated that oxygen nonstoichiometry corresponds to the generation of microphases $[Sr_8Fe_{12}O_{26}]$ $[Sr_2Fe_3O_6]_n$, whose first integral member $n = 1$, which corresponds to $p = 0.4$, is isolated here for the first time by synthesis under argon. Structural models involving intergrowths of single perovskite $[Sr_2Fe_2O_6]_\infty$ layers with complex $[Sr_2Fe_4O_{7-\delta}]_\infty$ layers involving two kinds of pyramidal ribbons, FeO_5 trigonal bi-pyramids and FeO_5 distorted tetragonal pyramids, explain the oxygen deficiency.

The numerous studies carried out for many years on the Sr−Fe−O system have shown its extraordinary richness, from the structural and the physical properties viewpoint. This is indeed exemplified by the oxygen-deficient perovskites and by the Ruddlesden−Popper phases, for which attractive magnetic properties such as negative magneto-resistance have been observed.[1−4] Besides those oxides, the compound $Sr_4Fe_6O_{13}$, reported more than 20 years ago,[5] is of great interest, owing to its mixed oxygen ion and electronic conductivity, which makes it a potential material for applications in the field of oxygen-selective membranes, especially when doped with cobalt.[6,7] The crystal structure[5,8] of this oxide was found to be derived from the perovskite structure, but curiously the different authors did not evidence any oxygen nonstoichiometry, in contrast to the other perovskites derivatives of this system. We have revisited the synthesis and crystal structure of this phase, using high-resolution electron microscopy (HREM). We show that this phase, when prepared in air or in an oxygen flow, is oxygen-deficient, that is, $Sr_4Fe_6O_{13-\delta}$, and exhibits a modulated structure. The modulation vector is $(p\vec{a}^* + q\vec{c}^*)$ with a p value of 0.47, instead of 0.50 for $\delta = 0$ and q close to 1. Analyzing the ideal structure of $Sr_4Fe_6O_{13-\delta}$, we demonstrate that the latter is a combination of two closely related "$Sr_4Fe_6O_{12}$" limit structures, so a series of modulated derivatives with the formulation $[Sr_8Fe_{12}O_{26}]$ $[Sr_2Fe_3O_6]_n$ should be generated, by introducing an oxygen deficiency. This viewpoint is strongly supported by the discovery of two other modulated structures, with $p = 0.45$ and 0.40, by working in reducing conditions.

Experimental Section

The polycrystalline single-phase sample was obtained from appropriate mixtures of SrO or $SrCO_3$ and Fe_2O_3, with a ratio Sr/Fe = 2/3. The intimately ground powders were then pressed in the form of bars. A first sample has been heated at 1100 °C for 24 h, reground, and reheated at 1100 °C for 24 h under air. In a second step, one sample with the same nominal composition has been heated at 900 °C for 24 h and 1100 °C for 24 h under N_2. Last, the first air-synthesized sample was reheated at 400 °C under Ar for 8 h, up to the stabilization of the TGA curve.

The samples for electron microscopy were prepared by crushing the crystals in butanol. The flakes in suspension are deposited onto a holey carbon film, supported by a copper grid. The electron diffraction (ED) investigation was carried out with a 2010 JEOL electron microscope. The reciprocal space was reconstructed by tilting around the crystallographic axes. The high-resolution electron microscopy (HREM) study was performed with a TOPCON 002B (V = 200 kV, Cs = 0.4 mm) and a JEOL FEG2011 (V = 200 kV, Cs = 1.4 mm). The three microscopes are equipped with energy dispersive spectroscopy (EDS) analyzers. Experimental HREM images were analyzed on the basis of theoretical images calculated for different focus and crystal thickness values, using the multislice method with the Mac Tempas software.

Sample purity was checked by X-ray diffraction using a PHILIPS vertical diffractometer PW1830 equipped with a graphite secondary monochromator and working with Cu Kα radiation.

Chemical titration and TGA analysis showed that the oxygen content of the air-synthesized sample was determined to be close to 13.

* Authors to whom correspondence should be addressed. E-mail: richard.retoux@ensicaen.fr or bernard.raveau@ensicaen.fr.

(1) Kanamuru, F.; Shimada, M.; Koizumi, M. *J. Phys. Chem. Solids* **1972**, *33*, 1169.
(2) Fjellvag, H.; Hauback, B. C.; Bredesen, R. *J. Mater. Chem.* **1997**, *7*, 2415.
(3) Bredesen, R.; Norby, T.; Bardal, A.; Lynum, V. *Solid State Ionics* **2000**, *135*, 687.
(4) Fossdal, A.; Sagdahl, L. T.; Einarsrisd, M. A.; Wiik, K.; Grande, T.; Larsen, P. H.; Poulsen, F. W. *Solid State Ionics* **2001**, *143*, 367.
(5) Yoshiasa, A.; Ueno, K.; Kanamuru, F. *Mater. Res. Bull.* **1986**, *21*, 175.
(6) Fjellvag, H.; Hauback, B. C.; Bredesen, R. *J. Mater. Chem.* **1997**, *7*, 2415.
(7) Fossdal, A.; Sagdahl, L. T.; Einarsrud, M. A.; Wiik, K.; Grande, T.; Larsen, P. H.; Poulsen, F. W. *Solid State Ionics* **2001**, *143*, 367.
(8) Ohkawa, M.; Fujita, S.; Takeno, S.; Nakatsuka, A.; Yoshiasa. *Z. Kristallogr.* **1997**, *212*, 848.

10.1021/cm040127d CCC: $27.50
Published on Web 10/16/2004

Results

Air-Synthesized $Sr_4Fe_6O_{13-\delta}$ ($\delta \approx 0.06$). The EDS analysis of more than 50 microcrystals of the air-synthesized sample of nominal composition $Sr_4Fe_6O_{13}$ shows the great homogeneity of the cationic distribution and confirms the "Sr_4Fe_6" composition, in the limits of accuracy of the technique. All the electron diffraction patterns of the different microcrystals can be described by a subcell derived from the perovskite, with $a \approx b \approx a_p\sqrt{2}$ and $c \approx 19$ Å, $\alpha \approx \beta \approx \gamma \approx 90°$ in agreement with previous results.[5−8] The lattice of this undistorted subcell is orthorhombic and the possible groups are *Fmmm*, *Fmm*2, or *F*222. A second set of rather intense extra reflections is also observed, as by previous authors,[5,8] but in contrast to the latter, these extra reflections do not correspond exactly to a doubling of the **a** parameter, but are in incommensurate positions so the present sample is characterized by a modulation vector ($p\vec{a}^* + q\vec{c}^*$), with average values close to $p = 0.47$ and $q \approx 1$, instead of $p = 0.50$ and $q = 1$ for the samples obtained by previous authors.[5,8] Moreover, one observes a different symmetry of the structure which is no more orthorhombic, but is lowered down to triclinic, with α, β, and γ close to 90°. Thus, the structure of this oxide can be described in the supercell with $a \approx (1/p)a_p\sqrt{2}$, $b \approx a_p\sqrt{2}$, $c \approx (1/q)19$ Å, $\alpha \approx \beta \approx 90°$, and $\gamma \approx 92°$. The lowering of the symmetry of the distorted modulated cell involves a loss of the mirrors but the ED patterns suggest that the translation relations of the face-centered structure are retained. In a simplifying aim, the real triclinic primitive cell is not considered herein but is described using a "nonstandard" setting of the cell with the super-space group *F*2/*m* (*p*0*q*). The ED patterns evidencing these modulations and subcell symmetries are presented in Figures 1 and 2.

The [001] ED patterns (Figure 1a) show the significant distortion of the subcell ($\gamma \approx 92°$) and the incommensurate value of the modulation by the splitting of the two spots around the forbidden *h*00 reflections (odd *h*) of the subcell. The modulation vector $p\vec{a}^*$ is parallel to the $\vec{a}^*_{subcell}$ axis, so these two spots are aligned along $\vec{a}^*$ and indexed 0002 and 200$\bar{2}$. The reflections conditions are *hk*0*m*: $k = 2n$, $m = 2n$ (see Figure 2a for the indexation of the satellites).

Two [010] patterns are given in Figures 1b and 1c for illustrating two examples of *q* value $q = 1$ and the other for *q* close but $\neq 1$:

$\Rightarrow$ $\boldsymbol{q = 1}$**,** in Figure 1b, the *m* suffix refers to the modulation vector $p\vec{a}^*$ parallel to the $\vec{a}^*_{subcell}$ axis. The 0002 and 200$\bar{2}$ spots are aligned along $\vec{a}^*$. The reflection conditions are *h*0*lm*: $h = 2n$ and $l + m = 2n$ (see Figure 2b for details on the reflection indexation).

$\Rightarrow$ $\boldsymbol{q = 1 - \epsilon}$**,** in Figure 1c, the *m* suffix refers to the modulation vector ($p\vec{a}^* + q\vec{c}^*$). The deviation of the amplitude of the modulation vector along $\vec{c}^*$ with regard to the value $q = 1$ clearly appears by viewing the two spots around the forbidden reflection (*h*00: $h = 2n+1$) of the subcell: they are not aligned along a direction parallel to $\vec{a}^*$ and are indexed 00$\bar{2}$2 and 202$\bar{2}$, the *m* indices referring to the vector ($p\vec{a}^* + q\vec{c}^*$). The reflection conditions are *h*0*lm*: $h = 2n$ and $l = 2n$, $\forall m$ (see Figure 2c for details on the reflection indexation).

Note that the two systems of reference, and consequently the *hklm* indexation, describe a unique modulated structure, the first one being a simpler particular case of commensurate $q = 1$ value. For all the samples presented herein, the ED patterns are characterized by *q* values equal to 1 or very close to 1 (i.e., $\epsilon \approx 0$), so for simplifying the description of the structures and nanostructures in the rest of the present paper, one shall only consider the first case, namely, the modulation vector $p\vec{a}^*$.

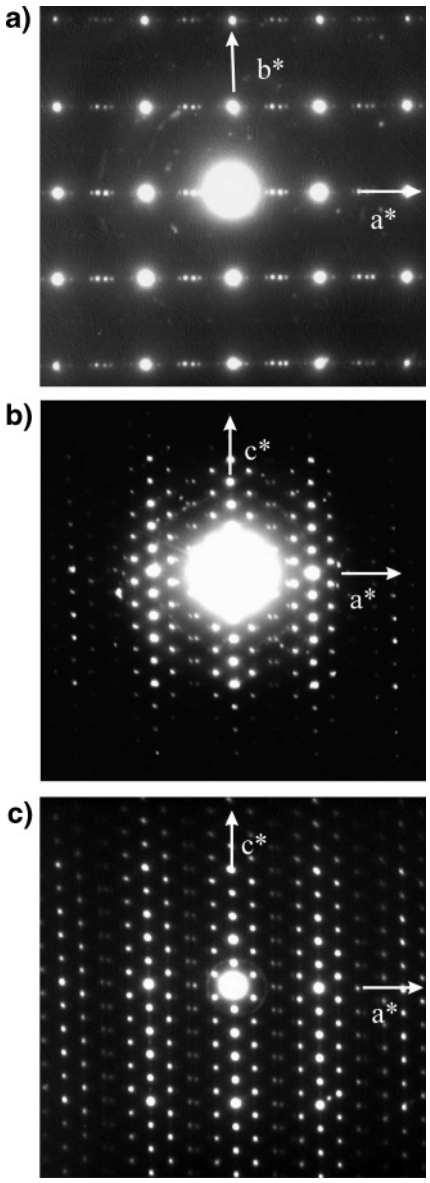

Figure 1. Air-synthesized sample: (a) [001] and (b) [010] ED patterns. (The modulation vector is $\approx 0.47\vec{a}^*$ and $q = 1$). (c) [010] ED patterns. (The modulation vector is $\approx 0.47\vec{a}^*$ and $q = 1 - \epsilon$).

The [010] HREM image of this air-synthesized phase (Figure 3) can partly be understood from the projection of the ideal structure of $Sr_4Fe_6O_{13}$ along $\vec{b}$ (Figure 4a), bearing in mind that the focus value of this HREM image is close to −550 Å, i.e., the bright dots are correlated to the high electron density zones. It has previously been reported that $Sr_4Fe_6O_{13}$ structure can be described by the stacking, perpendicularly to the layers, of one single perovskite layer with pyramidal iron layers Fe_2O_3.[5,8] In the latter papers, this perpendicular axis was denoted **b** by previous authors for $Sr_4Fe_6O_{13}$. Nevertheless, to ensure the continuity and

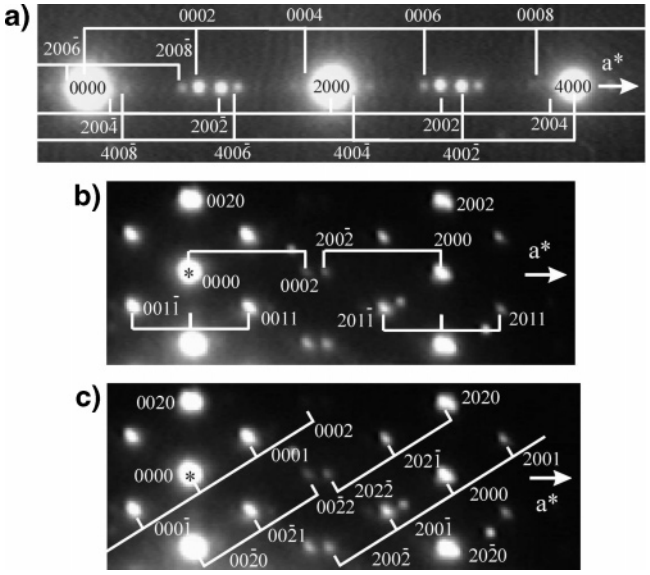

Figure 2. Indexation mode using *hklm*: [001] ED pattern (a) and [010] ED patterns for $q = 1$ (b) and $q \neq 1$ (c).

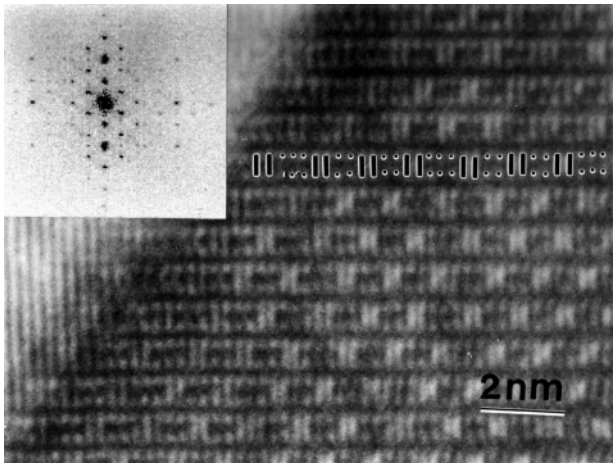

Figure 3. (a) Typical [010] HREM image of the [Air]-synthesized sample and (b) corresponding FFT.

comparison with other intergrowth structures, especially the Ruddlesden−Popper (RP) phases,[9] we prefer to describe this structure as the stacking along $\vec{c}$ of single $[Sr_2Fe_2O_6]_\infty$ perovskite layers with $[Sr_2Fe_4O_7]_\infty$ pyramidal layers (Figure 4a). The comparison of Figure 3 and Figure 4a clearly shows that in the present sample the $[SrO]_\infty$ layers are alternately spaced by 3.7 and 6.5 Å along the direction perpendicular to the layers, like in the "pure" $Sr_4Fe_6O_{13}$ structure. The 3.7 Å spacing can be then correlated to the perovskite layer as commonly observed in numerous RP phases[9] and the dark contrast between the 6.5 Å spaced $[SrO]_\infty$ layers suggests that the double layers of lighter elements correspond to the pyramidal iron layers. However, the examination of the $[Sr_2Fe_4O_7]_\infty$ pyramidal layers (Figure 4a) shows a greater complexity: the latter consists indeed of two sorts of pyramidal ribbons of edge-sharing pyramids running along $\vec{b}$: the first one, labeled $[Fe_2]_\infty^{BiP}$, consists of double rows of edge-sharing FeO_5 trigonal bipyramids whereas the second one labeled $[Fe_2]_\infty^{TeP}$ consists of double rows of distorted tetragonal pyramids (Figure 4b). In the ideal $Sr_4Fe_6O_{13}$ structure (Figure 4a)

(9) Ruddlesden, S. N.; Popper, P. *Acta Crystallogr.* **1958**, *11*, 54.

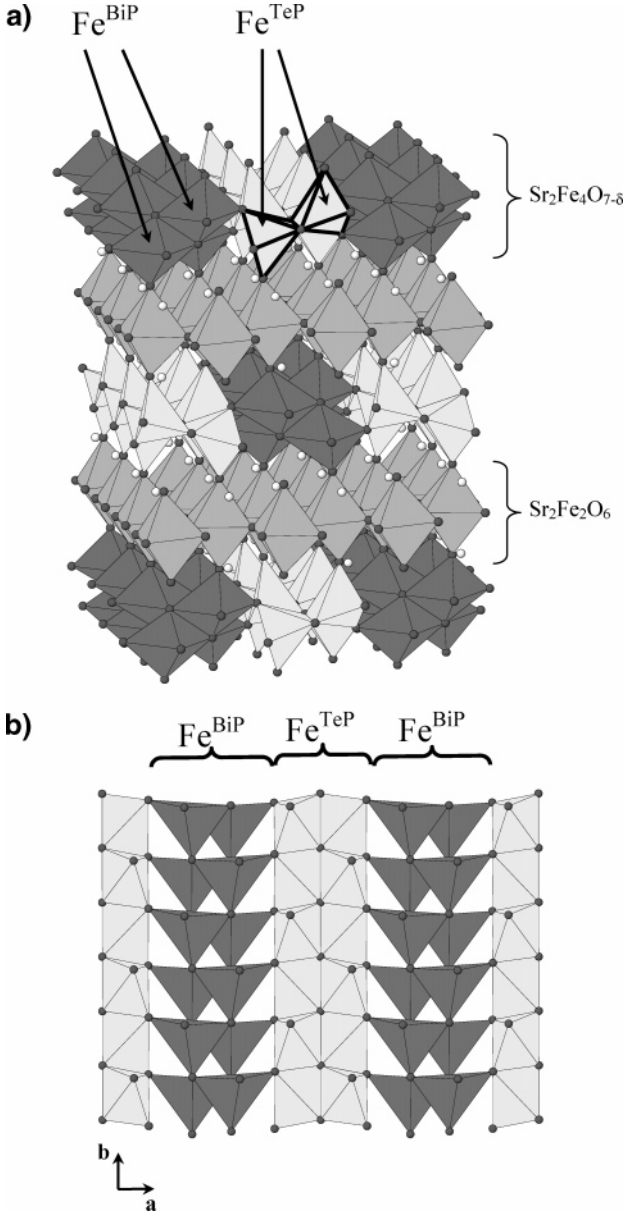

Figure 4. Structure of the ideal $Sr_4Fe_6O_{13}$: (a) along [010] and (b) drawing of the different ribbons viewed along [001].

one $[Fe_2]_\infty^{BiP}$ ribbon alternates with one $[Fe_2]_\infty^{TeP}$ ribbon along $\vec{a}$, so the contrast at the level of the $[Sr_2Fe_4O_7]_\infty$ layers should correspond to the following sequence along $\vec{a}$: two bright sticks spaced by about 2.9 Å (BiP rows) alternating with two couples of bright dots spaced by about 3.4 Å (TeP rows). In fact, for our sample (Figure 3), the contrast observed at the level of this layer shows that two and three couples of bright dots appear, distributed in a modulated manner along $\vec{a}$, according to the $p = 0.47$ periodicity. The FFT of the HREM zones is given in the insert in Figure 3. This suggests that triple ribbons of edge-sharing tetragonal pyramids $[Fe_3]_\infty^{TeP}$ replace periodically the double $[Fe_2]_\infty^{TeP}$ ribbons. It will be shown further that the oxygen stoichiometry is no more "O_{13}" but is oxygen-deficient.

Mechanism of Oxygen Nonstoichiometry in $Sr_4Fe_6O_{13-\delta}$: The Derivatives $[Sr_8Fe_{12}O_{26}]\cdot[Sr_2Fe_3O_6]_n$. Starting from the above description of the structure of $Sr_4Fe_6O_{13}$, two other limits structures with the same composition $Sr_2Fe_3O_6$ can be generated. The

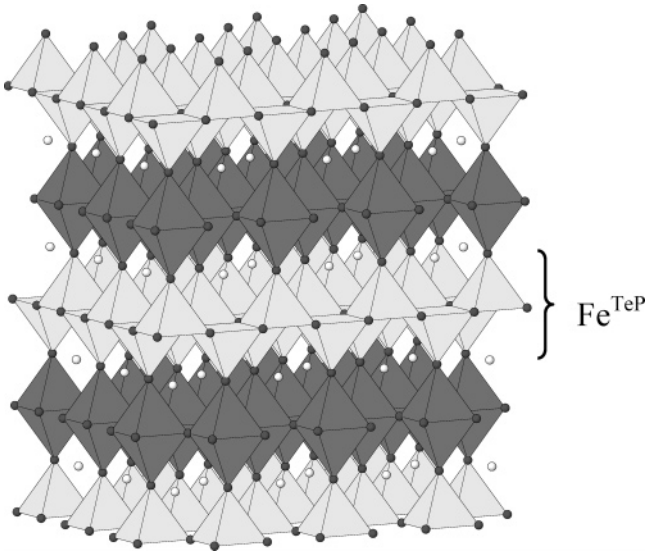

Figure 5. Ideal structures of the I-TePP limit model for $Sr_4Fe_6O_{12}$.

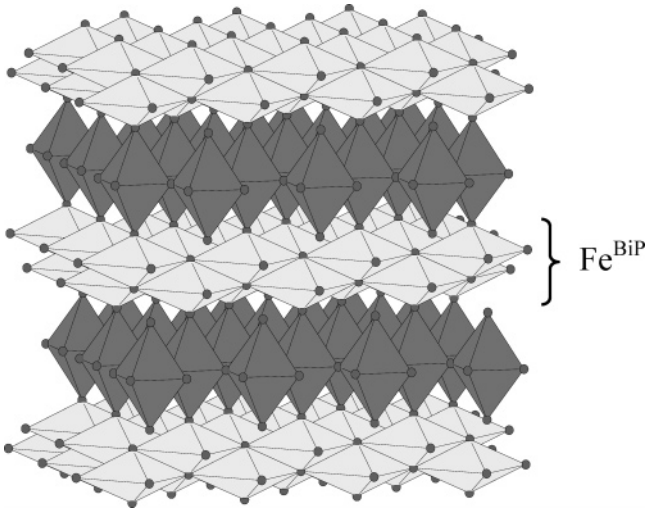

Figure 6. Ideal structures of the I-BiPP limit model for $Sr_4Fe_6O_{12}$.

first one (Figure 5) corresponds to the extension of the $[Fe_2]_\infty^{TeP}$ ribbons ad infinitum along $\vec{a}$, so $[Fe_2O_3]_\infty$ layers of edge-sharing FeO_5 tetragonal pyramids are formed, whose apexes are directed alternately up and down on each side of a $[Fe_2O_2]_\infty$ square planar lattice, adopting the configuration of the BiO_4 pyramids in the Aurivillius phases.[10] Along $\vec{c}$, the $[Fe_2O_3]_\infty$ layers and the $[FeO_3]_\infty$ octahedral layers share their apexes, forming an $[Fe_3O_6]_\infty$ 3D framework in which the Sr^{2+} cation is located, at the layer junction, leading to the $Sr_2Fe_3O_6$ ideal structure. Such a theoretical structure, which we call "I-TePP" (**I**ntergrowth between **Te**tragonal **P**yramids and **P**erovskite layers), will be difficult or may be impossible to stabilize due to the large mismatch between the perovskite layer ($a_p = 3.9$ Å) and the $[Fe_2O_2]_\infty$ rock salt layer ($a_{Fe} = 4.3$ Å), so the $[Fe_2O_3]_\infty$ layers should be strongly compressed, resulting in a puckering, already observed for the $[Fe_2]_\infty^{TeP}$ ribbons of $Sr_4Fe_6O_{13}$.[5,8] The second limit $Sr_2Fe_3O_6$ structure (Figure 6) corresponds to the extension of the $[Fe_2]_\infty^{BiP}$ ribbons ad infinitum along $\vec{a}$, resulting in the formation of $[Fe_2O_3]_\infty$ layers of edge-sharing trigonal bipyramids, whose longer apical bonds are directed along $\vec{a}$, with a configuration similar to that encountered in the hexagonal $YAlO_3$[11] and $LuMnO_3$ structure.[12] Along $\vec{c}$, the $[Fe_2O_3]_\infty$ layers and the $[FeO_3]_\infty^P$ layers share their apexes, forming an $[Fe_3O_6]_\infty$ 3D framework where the Sr^{2+}cations are inserted. This theoretical $Sr_2Fe_3O_6$ structure, called "I-BiPP" (**I**ntergrowth between **BiP**yramidal and **P**erovskite layers), will also be difficult or may be impossible to stabilize for the opposite reason to that evoked above. The "O−Fe−O" apical bonds of the bipyramid correspond to an average distance of about 4.6 Å, whereas the corresponding O−O distance in the perovskite structure is about 5.5 Å ($\sim a_p\sqrt{2}$). Thus, a large mismatch would also exist between the two layers, but in that case it would result in a dramatic expansion of the bipyramidal iron layer.

It is then easy to understand that the mismatch between the $[Sr_2Fe_4O_7]_\infty$ layers and the $[Sr_2Fe_2O_6]_\infty$ perovskite layers will be decreased by connecting the two sorts of $[Fe_2O_3]_\infty$ layers through the corners of their FeO_5 tetragonal pyramids and trigonal bipyramids. In that way the oxygen content will be increased with respect to the starting hypothetical $Sr_2Fe_3O_6$ structures. It results in the possible formation of a series of closely related microphases, with the generic formulation $[Sr_8Fe_{12}O_{26}][Sr_2Fe_3O_6]_n$. The model of one member of the family ($n = 0.5$) is given in Figure 7 for showing the $[Sr_2Fe_4O_{7-\delta}]_\infty$ and $[Sr_2Fe_2O_6]_\infty$ layers on one hand and, on the other hand, the $[Sr_8Fe_{12}O_{26}]$ and $[Sr_2Fe_3O_6]$ structural units. The trigonal bipyramids are schematically represented as vertical sticks and the tetragonal pyramids as double points in order to make easier further description of the HREM images.

The limit member $n = 0$, $Sr_8Fe_{12}O_{26}$, corresponds to the stoichiometric ideal $Sr_4Fe_6O_{13}$ and is made more stable by the fact that the mismatch between the $[Sr_2Fe_4O_7]_\infty$ and the $[Sr_2Fe_2O_6]_\infty$ layers is practically compensated by the juxtaposition of the $[Fe_2]_\infty^{TeP}$ to the $[Fe_2]_\infty^{BiP}$ ribbons, which are respectively larger and smaller than the periodicity of the perovskite layer. Then two types of structures can be proposed for the different n members of the series, as schematized in Figure 8. The two different pyramidals layers can be formulated $[Fe_2]_2^{BiP}[Fe_2]_{2+n}^{TeP}$ (Figures 8a and 8b) and $[Fe_2]_2^{TeP}[Fe_2]_{2+n}^{BiP}$ (Figure 8c), $n = \infty$ corresponding to the two types of layers, already described for the two different $Sr_2Fe_3O_6$ structures. In each of these series the increase of n by the step of one unity corresponds to the periodic addition of only one row $[Fe]_\infty$ either of edge-sharing tetragonal pyramids or of trigonal bipyramids. It is worth pointing out that the introduction of tetragonal pyramids tends to increase the parameter subcell, whereas in contrast the introduction of trigonal pyramids favors the relaxation of the cell. In any case, the oxygen content decreases as n increases. It is not possible to predict which of these models will be involved in the oxygen nonstoichiometry. In contrast, it is easy to identify from the HREM images what model is valid from the spacing of the bright spots along $\vec{a}$: the double

(10) Aurivillius, B. *Ark. Kemi* **1949**, *1* (54), 463.

(11) Giaquintaa, D. M.; zur Loye, H. C. *J. Am. Chem. Soc*. **1992**, *114*, 10952.

(12) Yakel, H. L.; Koehler, W. C.; Bertaut, E. F.; Forrat, E. F. *Acta Crystallogr.* **1963**, *16,* 957.

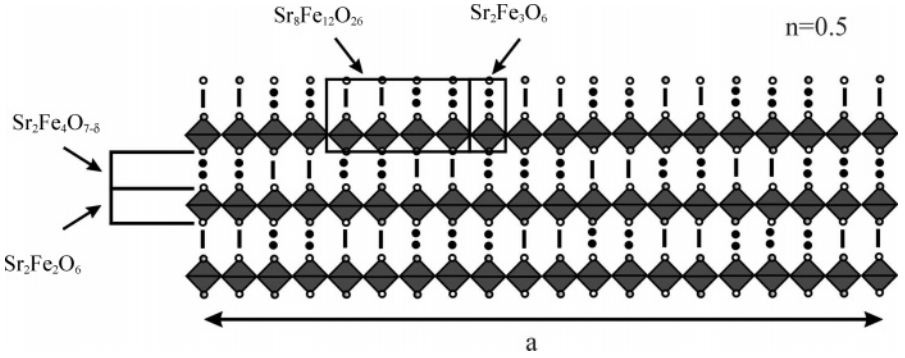

Figure 7. Idealized model of one $n = 0.5$ member, showing the $[Sr_2Fe_4O_{7-\delta}]_\infty$ and $[Sr_2Fe_2O_6]_\infty$ layers, the $[Sr_8Fe_{12}O_{26}]$ and $[Sr_2Fe_3O_6]$ structural units. The trigonal bipyramids are represented as vertical sticks and the tetragonal pyramids as double points.

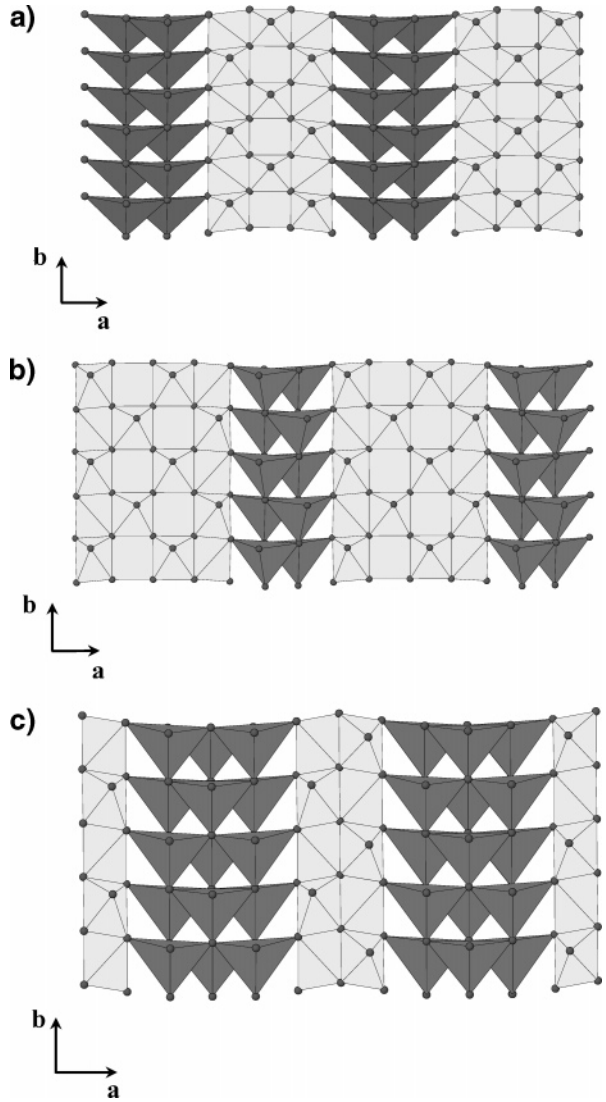

Figure 8. Idealized models of the family $[Fe_2]_2^{BiP}[Fe_2]_{2+n}^{TeP}$: (a) $n = 1$, (b) $n = 2$, and (c) $n = 1$ of the family $[Fe_2]_2^{TeP}$-$[Fe_2]_{2+n}^{BiP}$.

sticks are indeed closer to each other for the $[Fe_2]_\infty^{BiP}$ ribbons (2.9 Å) than for the $[Fe_2]_\infty^{TeP}$ ribbons (3.4 Å). Thus, in the case of our air-synthesized oxide, the appearance of triple ribbons $[Fe_3]_\infty$ spaced by 3.4 Å shows that the first mechanism involving the addition of rows of tetragonal pyramids (Figures 8a and 8b) takes place. In fact, the nonintegral n values correspond to the modulated distribution of the multiple $[Fe_n]_\infty^{TeP}$ ribbons in the structure, characterized by the modulation vector. Thus, the modulation vector $p\vec{a}$ is related to n by the relation $p = 2/(4 + n)$, so the $n = 1, 2, 3$ layers correspond to p values of 2/5, 1/3, and 2/7, respectively. Three examples of idealized modes are given in Figure 8; the idealized models of the $n = 1$ and $n = 2$ members of the family $[Fe_2]_2^{BiP}[Fe_2]_{2+n}^{TeP}$ are drawn in Figures 8a and 8b, respectively, and the $n = 1$ member of the family $[Fe_2]_2^{TeP}[Fe_2]_{2+n}^{BiP}$ in Figure 8c. If one admits that the perovskite layer does not exhibit any oxygen deficiency as previously shown for $Sr_4Fe_6O_{13}$,[5,8] the oxygen deficiency in these compounds formulated $Sr_4Fe_6O_{13-\delta}$ can be related to the modulation vector by the expression $p = (1 - \delta)/2$. Thus, it is easy to understand that our air-synthesized phase $Sr_4Fe_6O_{13-\delta}$ ($p = 0.47$) exhibits a very small oxygen deficiency, $\delta = 0.06$, which cannot be detected by chemical analysis.

Finally, the crystallographic parameters of the oxygen-deficient microphases $[Sr_8Fe_{12}O_{26}]\cdot[Sr_2Fe_3O_6]_n$ can be predicted for the different n values. Accounting that the modulation results from the difference in width (along $\vec{a}$) and in height (along the [001] direction of the $n = 0$ member, $Sr_4Fe_6O_{13}$, and labeled along $\vec{c}_0$) between the two different types of ribbons, the high flexibility of the perovskite layer allows accommodation of this disparity, through a strong waving of the layers. The way to decrease the strain effect is an antiphase array of the nodes in the adjacent layers along $\vec{c}_0$.

→ For the **integer even n** members: the nodes can adopt the antiphase arrangement. The most likely translation of the first adjacent layer is $(2 + n/2)\vec{a}_p(\sqrt{2}/2)$.

The most symmetric cell is orthorhombic and B-centered with the following parameters: $a = 2a_p\sqrt{2} + na_p(\sqrt{2}/2)$, $b = a_p\sqrt{2}$, and $c_n \approx c_0 \approx 19$ Å $\approx 2(a_p + 6.5$ Å).

→ For the **integer odd n** members: the nodes cannot be in an antiphase array anymore with two different possibilities:

If $[(n + 1)/2)]$ is odd, the most likely translation of the first adjacent layer is $\{(\vec{c}_0/2) + [(n + 5)/2]\vec{a}_p(\sqrt{2}/2)\}$. The cell is monoclinic with $a_n = 2(2a_p\sqrt{2} + na_p(\sqrt{2}/2))$, $b_n = a_p\sqrt{2}$, $c_n = [c_0/(2\cos(\beta - 90°))]$, and tg $\beta = (n + 5)[(a_p\sqrt{2})/c_0)$.

If $[(n + 1)/2]$ is even, the most likely translation of the first adjacent layer is $\vec{c}_0/2 + [(n + 3)/2]\vec{a}_p(\sqrt{2}/2)$. The cell is monoclinic with $a_n = 2(2a_p\sqrt{2} + na_p(\sqrt{2}/2))$, $b_n = a_p\sqrt{2}$, $c_n = [c_0/(2\cos(\beta - 90°))]$ and tg $\beta = (n + 3)(a_p\sqrt{2}/c_0)$.

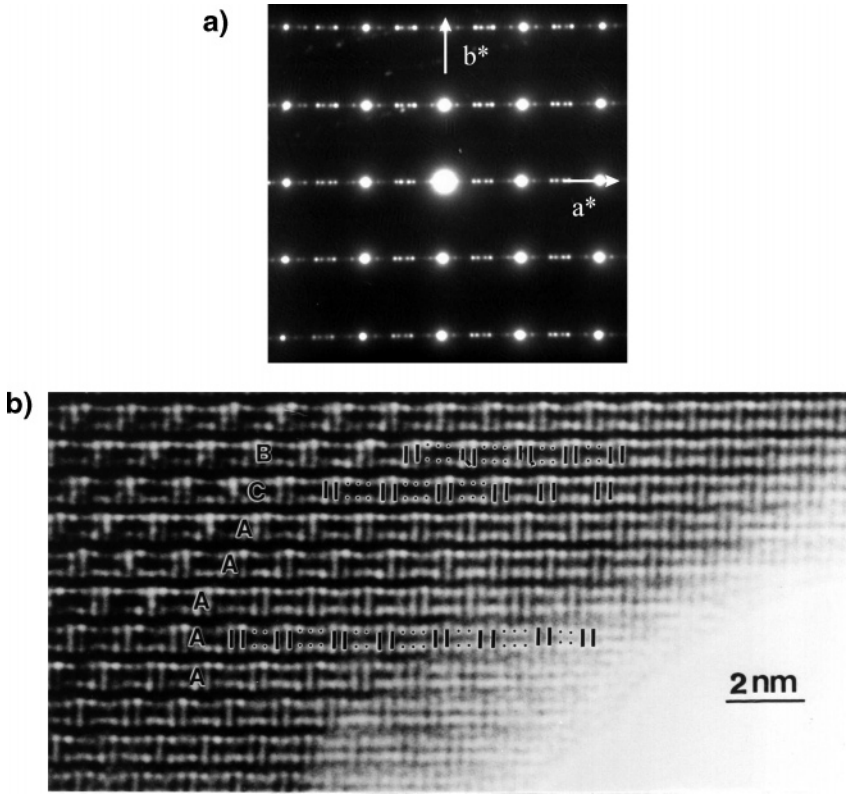

Figure 9. [N_2] sample: (a) [001] ED pattern and (b) [010] HREM image. (The modulation vector is $\approx 0.44\vec{a}^*$.)

→ For the **noninteger *n* values**, associated with regular sequences of $[Fe_2]^{TeP}$ and $[Fe_2]^{BiP}$, the a parameter is calculated considering a supercell of a "N" member, N being the lower integer closest to $1/n$. The amplitude of the modulation vectors along $\vec{c}^*$, $q = 1$ or $\neq 1$ (see above section), depends in a complex manner on the sequence of the $[Fe_2]^{TeP}$ and $[Fe_2]^{BiP}$ along $\vec{a}$ and on the translation of this arrangement in the adjacent slices, leading to a huge number of possibilities for the supercells.

Generalization: Detailed HREM Study of Several Reduced Samples. To check the above models, a systematic HREM study has been carried out, varying the synthesis conditions, especially the gas atmosphere.

The sample synthesized under nitrogen flow is also single-phased. The average p value is close to $0.44 \approx 4/9$. One example of a [001] ED pattern is given in Figure 9a. On the basis of the aforementioned $p = 2/(4 + n)$ relationship, such a p value corresponds to $n = 0.5$. The ideal model for this noninteger n value would correspond to the intergrowth along [100] of one $n = 0$ and one $n = 1$ member. A typical HREM image of this [N_2] sample is displayed in Figure 9b (same focus value as above). The sequence of [2 bright sticks/2 couples of bright dots] − [2 bright sticks/3 couples of bright dots], corresponding to the $n = 0$ and $n = 1$ members, respectively, is perfectly established in the zone labeled **A**. Since n is noninteger, a supercell must be considered with $a \approx 18a_p(\sqrt{2}/2)$. The translation in the adjacent layers along $\vec{c}_0$ is regular, so the supercell is monoclinic with $b_{mono} = a_p\sqrt{2}$, $c_{mono} = [c_0/(2\cos(\beta - 90°))]$ and $\beta \approx 120°$. In the layers labeled **B** and **C**, the sequences along [100] are more complex but always built of $n = 0$ and $n = 1$ members. In the layer **B**, the inversion of one [$n = 0$] and [$n = 1$] members induces the local sequence [$n = 0$] [$n = 0$] [$n = 1$] [$n = 1$], keeping the same "local" composition whereas in the layer **C**, three adjacent [$n = 1$] members are observed. This example shows that for given n and p values, there exist different associations of the limit integer members. In the present case, the $n = 0.5$ member is built up from the intergrowth of $n = 0$ and $n = 1$ members. The most regular arrangement induces a monoclinic supercell (zone **A**), but these images show that there obviously exists an infinity of more complex combinations.

For the sample annealed under A_r/H_2 at 400 °C, the average p value is close to 0.4, i.e., corresponds to the ideal value of the $n = 1$ member of the series. The HREM images of the $n = 1$ member are characterized by the typical contrast of two bright sticks separated by three couples of bright dots, associated with the sequence of two $[Fe_2]^{BiP}$ and three $[Fe_2]^{TeP}$. All the $[Sr_8Fe_{12}O_{26}]$ $[Sr_2Fe_3O_6]_\infty$ slices are similar and rather regular. The important point observed for this regular odd $n = 1$ member is a variation in the sequence of the translation of the adjacent layers along [001]. The expected translation of the two $[Fe_2]^{BiP}$ and three $[Fe_2]^{TeP}$ in the adjacent layer is $\vec{t} = a_p\sqrt{2}$. The parameters of the above-described simple monoclinic cell can be calculated; they are therefore $a_n \approx 14$ Å, $b_n \approx 5.6$ Å, $c_n \approx 19$ Å, and $\beta \approx 120°$, as experimentally observed (Figure 11) in the zone labeled **M** and schematically drawn in Figure 10b. However, in the zone labeled **O**, a chemical twinning phenomenon can be clearly observed. This phenomenon shows that the first adjacent layer suffers the translation $\vec{t}$ but that the second adjacent layer is translated by $-\vec{t}$, in a regular manner (Figure 10c). Such a mechanism, called chemical twinning, involves the formation of an orthorhombic double cell with $a_{ortho} \approx 14$ Å, $b_{ortho} \approx 5.6$ Å, and $c \approx 19$ Å as

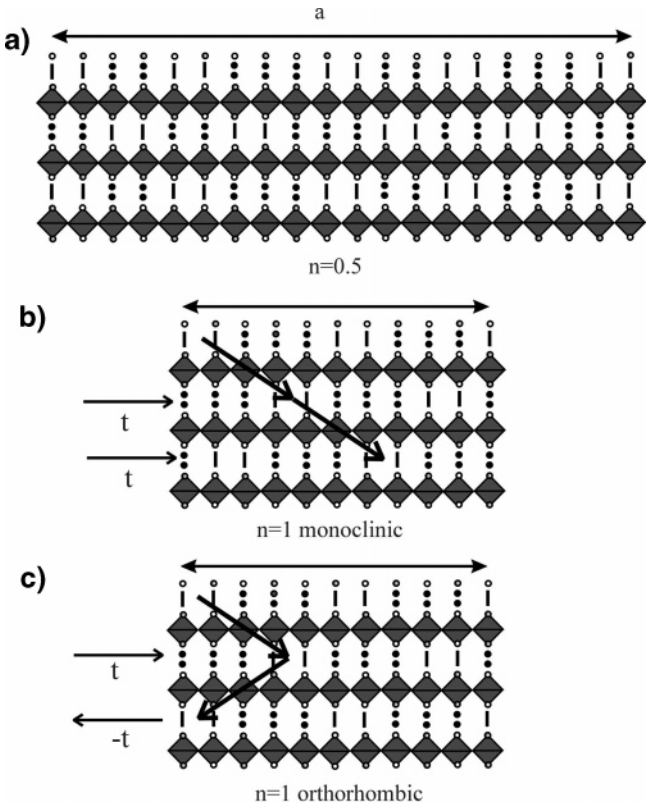

Figure 10. Structures and corresponding image contrast are schematically drawn: (a) $n = 0.5$, (b) monoclinic $n = 1$, and (c) orthorhombic $n = 1$. The two $n = 1$ models are correlated by chemical twinning phenomena.

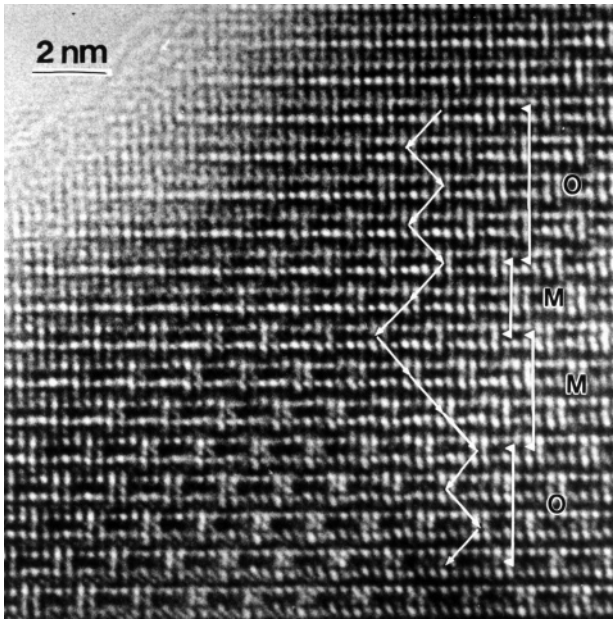

Figure 11. [Ar/H_2] sample: [010] ED pattern and (b) [010] HREM image. (The modulation vector is $\approx 0.4\vec{a}^*$).

experimentally observed in the zone **O** and schematically drawn in Figures 11 and 10c, respectively.

The ED pattern and image, recorded for a reduced [A_r/H_2] sample and displayed in Figure 12, are the last examples presented herein for illustrating the complex structural family. The ED pattern is characterized by the superimposition of two systems of satellites and diffuse streaks. The amplitude of the modulation vectors show that the first system corresponds to $p = 0.4$, that

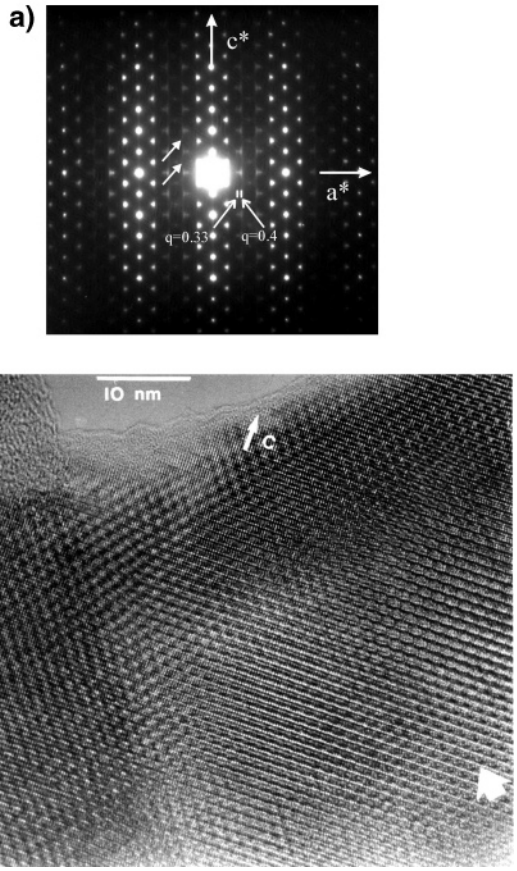

Figure 12. Example of complex [010]: (a) ED pattern and (b) overview HREM image of a reduced sample.

is, $n = 1$ presented above and the second to $p = 0.33$, that is, the $n = 2$ member which is the highest n value obtained in our synthesis conditions. The first system of diffuse intensity (white arrows in Figure 12a) is observed along well-defined loci and can be attributed to a transition state[13,14] between SRO (short range ordering) and LRO (long range ordering) of the $n = 1$ and $n = 2$ members. The second diffuse intensity appears as streak lines along c^* and are attributed to the stacking defect along the direction perpendicular to the layers as shown in the HREM images (Figure 12b). One observes the local formation of small domains in zones of random sequences of different members. This is clearly observed by viewing the image at grazing incidence, along oblique directions with regard to $\vec{c}$ (pointed out by large arrows).

Concluding Remarks

The electron diffraction and high-resolution electron microscopy of different $Sr_4Fe_6O_{13-\delta}$ samples shows that these oxides exhibit complex modulated structures, with modulation vectors $(p\vec{a}^* + q\vec{c}^*)$, $p = (1 - \delta)/2$ varying in the range [0.4−0.5] and $q \approx 1$. The oxygen nonstoichiometry induces the generation of microphases $[Sr_8Fe_{12}O_{26}].[Sr_2Fe_3O_6]_n$, resulting from intergrowths of the single perovskite layers with a complex $[Sr_2Fe_4O_{7-\delta}]_\infty$ layer involving two kinds of pyramidal ribbons FeO_5

(13) de Ridder, R.; Van Tendeloo, G.; Amelinckx, S. *Acta Crystallogr.* **1976**, *A32*, 216.
(14) Van Tendeloo, G.; Amelinckx, S. *Phase Transitions* **1998**, *67*, 101.

trigonal bipyramids and FeO_5 distorted tetragonal pyramids. Such a complex structural mechanism clearly opens the route to a huge family of new materials, resulting from a double mechanism of intergrowth:

(i) The intergrowth along $\vec{a}$ of the $[Fe_2]^{BiP}$ and $[Fe_2]^{TeP}$ units to form a complex pyramidal layer $[Sr_2Fe_4O_{7-\delta}]_\infty$, the different n members having the formulation $[Sr_4Fe_8O_{14}]\cdot[SrFe_2O_3]_n$.

(ii) The intergrowth along $\vec{c}$ of the different $[Sr_4Fe_8O_{14}]\cdot[SrFe_2O_3]_n$ pyramidal layers with m $[Sr_2Fe_2O_6]_\infty$ perovskite layers, involving a perovskite slice having the formulation $[Sr_{4+n}Fe_{4+n}O_{12+3n}]_m$.

From the present results, the oxygen nonstoichiometry clearly appears to be one of the key factors for the stabilization of the microphases. Nevertheless, the important mismatch between the pyramidal ribbons FeO_5 trigonal bipyramids and FeO_5 distorted tetragonal pyramids and perovskite layers, which is responsible for the strong displacive modulation, is undoubtedly another important parameter, which must be taken into account, especially for the actual iron coordination. This complex coordination is probably the key to the understanding of these nanostructures.

Acknowledgment. The authors gratefully acknowledge the European Union (FEDER), the Regional Council of Basse-Normandie, the CNRS (Centre National de la Recherche Scientifique), and the Ministry of Research for financial support.

Note Added in Proof

During the writing of this paper, the authors were informed that closely related phenomena were observed on thin films by G. Van Tendeloo et al.

CM040127D